



An Intermetallic CaFe_6Ge_6 Approach to Unprecedented Ca–Fe–O Electrocatalyst for Efficient Alkaline Oxygen Evolution Reaction

Hongyuan Yang,^[a] J. Niklas Hausmann,^[a] Viktor Hlukhyy,^[b] Thomas Braun,^[b] Konstantin Laun,^[c] Ingo Zebger,^[c] Matthias Driess,^[a] and Prashanth W. Menezes^{*[a, d]}

Based on the low-cost and relatively high catalytic activity, considerable efforts have been devoted towards developing redox-active transition metal (TM)-oxygen electrocatalysts for the alkaline oxygen evolution reaction (OER) while the role of redox-inactive alkaline earth metals has often been neglected in OER. Herein, for the first time, we developed a novel ternary intermetallic CaFe_6Ge_6 precatalyst, whose surface rapidly transforms into a porous ultrathin Ca–Fe–O heteroshell structure during alkaline OER through the oxidative leaching of surficial

Ge. Benefiting from synergistic effects, this highly efficient OER-active material with distinct Ca–Fe–O layers has a large electrochemical surface area and more exposed active Fe sites than a Ca-free FeO_x phase. Also, the presence of Ca in Ca–Fe–O is responsible for the enhanced transport and activation of hydroxyls and related OER reaction intermediate as unequivocally illustrated by a combination of quasi in-situ Raman spectroscopy and various ex-situ methods.

Introduction

The rapidly growing energy consumption and environmental problems have propelled the development of hydrogen (H_2) energy.^[1,2] Compared with the traditional H_2 production methods based on fossil fuels, water electrolysis is more promising as it can provide a sustainable and clean H_2 fuel, to solve the global environmental pollution and energy demand in the future.^[3–5] For electrocatalytic water splitting, the anodic half-reaction, the oxygen evolution reaction (OER), has been the bottleneck for the overall reaction efficiency. This is because the

OER involves complicated four-electron and proton transfers with multiple high-energy reaction intermediates, thereby being kinetically and thermodynamically sluggish.^[6,7] Although noble metal-based catalysts have been developed and commercialized to accelerate the OER, their high cost and extreme scarcity limit their application.^[8,9] Conversely, inexpensive and earth-abundant non-noble metal catalysts, especially redox-active TM-oxide-based compounds have been extensively developed as efficient electrochemical OER catalysts.^[10,11] Nevertheless, the role of redox-inactive alkaline earth metals for electrocatalytic water oxidation has long been underestimated. Intriguingly, several works on Ca-containing TM-oxido compounds have emphasized the significant role of Ca in promoting photochemical water oxidation, particularly its binding and activation effect towards H_2O molecules.^[12–14] Nonetheless, to the best of our knowledge, such compounds have been hardly explored for electrocatalytic OER in an alkaline environment. Aiming at this condition, only a very limited amount of Ca-containing Mn-based oxides and some perovskite-type TM oxides^[15–18] have been studied, which show low catalytic efficiency.^[17–20] Consequently, the role of Ca^{II} ions in accelerating the electrocatalytic alkaline OER process is still under debate. Notably, Yang *et al.* recently utilized both results from theoretical calculations and experiments to testify that the introduction of Lewis acidic species can enhance the adsorption of hydroxyl promoting alkaline OER activity.^[21] Considering that Ca can serve as Lewis acid for photocatalytic OER,^[20] it probably can also play a promotor role in electrochemical alkaline OER.


Over the past few years, Fe-based compounds have been regarded as one of the most promising candidates for electrocatalytic OER owing to the large abundance of Fe in the earth crust, accessible flexible redox states, as well as its rich coordination chemistry. Nevertheless, those compounds are known to transform into the corresponding Fe-based


[a] H. Yang, J. N. Hausmann, Prof. M. Driess, Dr. P. W. Menezes
Department of Chemistry: Metalorganics and Inorganic Materials
Technical University of Berlin
Straße des 17 Juni 135, Sekr. C2
10623 Berlin (Germany)
E-mail: prashanth.menezes@mailbox.tu-berlin.de

[b] Dr. V. Hlukhyy, T. Braun
Department of Chemistry
Technical University of Munich
Lichtenbergstraße 4
85747 Garching (Germany)

[c] K. Laun, Dr. I. Zebger
Department of Chemistry: Physical Chemistry/Biophysical Chemistry
Technische Universität Berlin
Straße des 17 Juni 135, Sekr. PC14
10623 Berlin (Germany)

[d] Dr. P. W. Menezes
Materials Chemistry Group for Thin Film Catalysis – CatLab
Helmholtz-Zentrum Berlin für Materialien und Energie
Albert-Einstein-Str. 15
12489 Berlin (Germany)
E-mail: prashanth.menezes@helmholtz-berlin.de

 Supporting information for this article is available on the WWW under <https://doi.org/10.1002/cctc.202200293>

 © 2022 The Authors. ChemCatChem published by Wiley-VCH GmbH. This is an open access article under the terms of the Creative Commons Attribution License, which permits use, distribution and reproduction in any medium, provided the original work is properly cited.

(oxy)hydroxides as real active structures during alkaline OER catalysis.^[22–24] Moreover, the relatively low intrinsic conductivity and activity of the pure Fe-based (oxy)hydroxides hamper the application of Fe-based electro(pre)catalysts in OER.^[25,26] As we have shown previously, binary Fe-based intermetallic compounds can exhibit much improved electrical conductivity and catalytic activity owing to a rapid corrosion of another metal component, which leads to a distinct structure composed of Fe-based extremely conductive intermetallic core with Fe-based (oxy)hydroxide shell comprising of large specific surface area and high porosity.^[24,25,27,28] This raised the next research question of whether a Fe-based intermetallic compound with more components (ternary or even more) would favor a more unique transformation to higher performing catalysts during the OER.

Considering the facile synthetic access, high metallic property, and structural reconstruction capability of TM-based intermetallic germanides to afford excellent OER catalysts^[27,29] through oxidative leaching of Ge, multinary germanides appear as suitable materials to try to answer the aforementioned research question. It was shown that, under alkaline OER corrosion conditions, Ge dissolves from the surface of the precatalyst as germanate (GeO_3^{2-}), thus leaving behind porous and amorphous TM-based (oxy)hydroxides. The latter leaching process can either be complete or incomplete (core-shell) depending upon the chemical resistance of the intermetallics. Such active structures could lead to a boosted system with enhanced electron transfer capability, easier electrolyte penetration, and more exposed active Fe sites to enable superior OER activity.^[27]

In this report, we would like to stress the following research questions: (i) can one synthesize a ternary Ca–Fe-based intermetallic germanide as a suitable precatalyst for electrochemical alkaline OER, and if so, (ii) can the precatalyst be transformed to amorphous or crystalline Ca-containing Fe-based (oxy)hydroxides (*i.e.*, Ca–Fe–O heterostructures) during OER? If yes, (iii) what is the role of Ca ions in such Ca–Fe–O compounds, (iv) whether and how does the presence of Ca enhance the OER activity, and finally, (v) what is the mechanism of such a Ca–Fe–O catalyst for OER in alkaline media?

In fact, we were able to synthesize the ternary intermetallic CaFe_6Ge_6 compound, which served as a suitable precatalyst for alkaline OER. During OER, under rapid leaching of Ge, CaFe_6Ge_6 transformed into a unique core-shell structure, where a porous Ca–Fe–O ($\alpha\text{-Fe}^{\text{III}}\text{OOH}@CaCO_3$) heteroshell was combined with the remaining intermetallic CaFe_6Ge_6 core. Benefiting from the fact that Lewis-acidic Ca^{II} ions can bind and transport hydroxyls,^[20,21] the stable carbonates acted as proton acceptors and promoted the formation of O–O bonds.^[30,31] On the contrary, Ge leaching induced high porosity and large specific surface area resulting in more exposed active Fe sites, and the intimately coupled electrical conducting intermetallic CaFe_6Ge_6 accelerated electron transfer. Thus, the formed Ca–Fe–O heterostructure exhibited excellent OER activity, especially when deposited on nickel foam (NF) under ambient air where the integrated electrode

delivered 100 mA cm^{-2} at an overpotential of only 322 mV with appreciable long-term stability. The herein achieved OER activity not only surpassed those of noble metal-based IrO_2 , various Fe-based (oxy)hydroxides, and binary Fe germanides, but also outmatched the same electrode under CO_2 -free electrolyte (where no CaCO_3 formed) in identical conditions.

Results and Discussion

Structural characterization of CaFe_6Ge_6

Ternary CaFe_6Ge_6 was synthesized using arc melting and subsequent annealing (see *Supporting Information*). It crystallizes in a TbFe_6Sn_6 -type structure with the orthorhombic space group $Cmcm$ (No. 63) and the lattice parameters of $a = 8.150\text{ \AA}$, $b = 17.698\text{ \AA}$, $c = 5.116\text{ \AA}$ (Figure 1a and Figure S1), representing an ordering variant of the $\text{Y}_{0.5}\text{Co}_3\text{Ge}_3$ -type. The structure of CaFe_6Ge_6 consists of Kagomé and graphene-like honeycomb layers of Fe and Ge atoms, respectively, alternately stacked along the a -axis. They form an edge-sharing trigonal-bipyramidal Fe_6Ge_4 framework with hexagonal channels which are filled alternately with isolated Ca atoms and Ge–Ge dumbbells. The phase purity of the as-prepared CaFe_6Ge_6 was then evaluated by a series of characterizations, including powder X-ray diffraction with Rietveld refinement (PXRD, Figure S2), inductively coupled plasma atomic emission spectroscopy (ICP-AES) (Table S1), scanning electron microscopy (SEM) with energy-dispersive X-ray (EDX) mapping (Figure 1b–e, Figure S3–S5, and Table S1), transmission electron microscopy (TEM) with high-resolution images and selected area electron diffraction (HRTEM and SAED, Figure 1f–g and Figures S6), as well as X-ray photoelectron spectroscopy (XPS, Figure S7). All data are consistent with the formation of pure CaFe_6Ge_6 phase.

Electrocatalytic OER activity

To explore the electrochemical performance of CaFe_6Ge_6 -derived Ca–Fe–O heterostructure, we deposited the well-defined CaFe_6Ge_6 on NF ($\text{CaFe}_6\text{Ge}_6/\text{NF}$) using Nafion binders (Figure S8–S11) and cycled it in a typical three-electrode cell configuration using cyclic voltammetry (CV). Compared with the 1st CV cycle, the activity of $\text{CaFe}_6\text{Ge}_6/\text{NF}$ was slightly enhanced during the course of anodic activation (the 5th cycle, Figure 2a). In particular, a 24 h chronoamperometry (CA) test of $\text{CaFe}_6\text{Ge}_6/\text{NF}$ at a constant potential of 1.515 V (vs reversible hydrogen electrode, RHE) showed initially increased and then stabilized current density. Similar to previously reported Fe-based intermetallic OER electro(pre)catalysts,^[24,25,27,28] this work also indicated the surface reconstruction of CaFe_6Ge_6 into Fe-based (oxy)hydroxides (Ca–Fe–O in this case). The activation process was completed after 24 h leading to better OER activity (inset of Figure 2a), which can also be confirmed by the post CA-CV with notably improved activity. More importantly, the post $\text{CaFe}_6\text{Ge}_6/\text{NF}$ possessed a double-layer capacitance (C_{dl}) value of

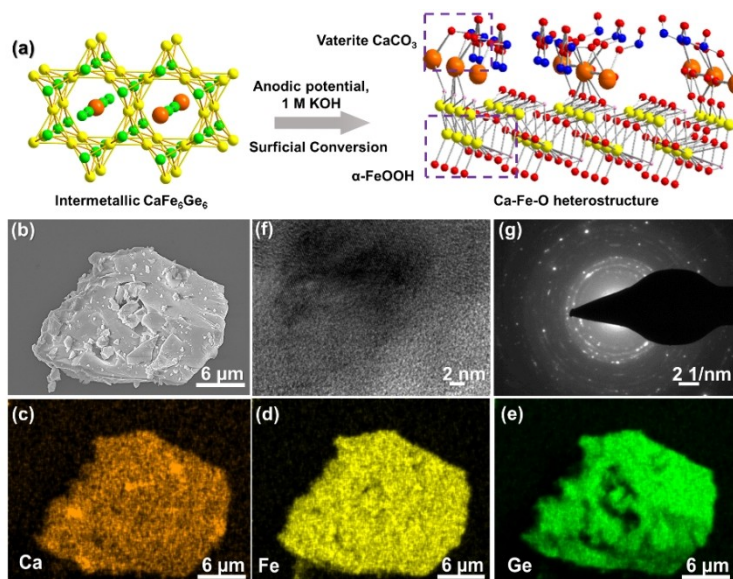


Figure 1. (a) Crystal structures of CaFe_6Ge_6 and Ca-Fe-O ($\alpha\text{-Fe}^{\text{III}}\text{OOH}@/\text{CaCO}_3$) heterostructure, as well as the illustration of their transformation. Note that the orange, yellow, green, blue, red, and pink spheres represent Ca, Fe, Ge, C, O, and H atoms, respectively. (b) SEM image and (c–e) EDX mapping of the CaFe_6Ge_6 particle with a homogeneous distribution of elements. (f) HRTEM image with the associated (g) SAED pattern showing the highly crystalline nature of CaFe_6Ge_6 .

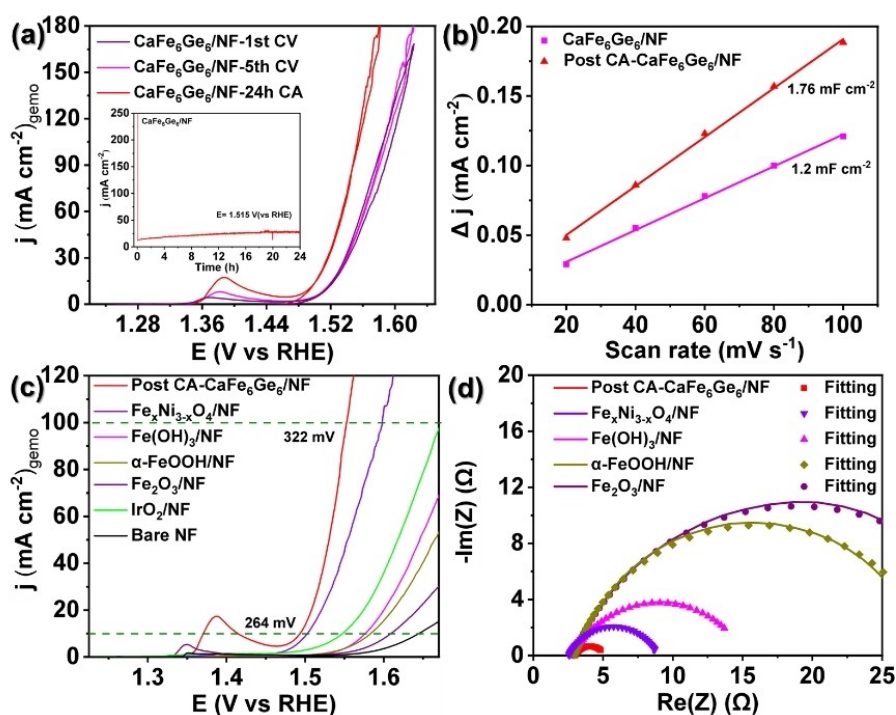


Figure 2. (a) The CV curves of $\text{CaFe}_6\text{Ge}_6/\text{NF}$ after 1st and 5th CV cycles, as well as 24 h CA (inset) at 1.515 V (vs RHE) in 1 M KOH electrolyte. (b) The C_{dl} values of $\text{CaFe}_6\text{Ge}_6/\text{NF}$ before and after 24 h CA calculated from their associated CV curves at non-Faradic regions. (c) LSV curves normalized against the geometric area of post CA- $\text{CaFe}_6\text{Ge}_6/\text{NF}$, Fe-based (oxy)hydroxides on NF, IrO_2/NF , and bare NF at a scan rate of 5 mV s^{-1} in 1 M KOH electrolyte. (d) Nyquist plot of post CA- $\text{CaFe}_6\text{Ge}_6/\text{NF}$ and Fe-based (oxy)hydroxides on NF obtained from EIS fitting to an equivalent circuit (inset) at an anodic potential of 1.53 V (vs RHE).

1.76 mF cm^{-2} (Figure S12 and Figure 2b), which was around 1.5 times larger than that of prior CA (1.2 mF cm^{-2}). Considering the value of double-layer capacitance (C_{dl}) is linearly proportional to

their electrochemically active surface areas (ECSA), this does further illustrate the distinct surface transformation of CaFe_6Ge_6 under anodic activation, thereby exposing a larger active

surface area for OER. To verify the excellent catalytic capability of such *in-situ* formed Fe-based (oxy)hydroxide, the directly synthesized and deposited reference Fe structures (low-crystallinity Fe(OH)₃ and crystalline α -FeOOH, Fe₂O₃, Fe_xNi_{3-x}O₄, S13–S16), as well as the noble metal-based IrO₂ on NF by testing them under the same conditions. The linear sweep voltammetry (LSV) clearly demonstrated that post CA-CaFe₆Ge₆/NF exhibited distinctly superior OER activity, delivering a current density of 10 and 100 mA cm⁻² at only 264 and 322 mV, superior to that of IrO₂/NF (316 and 443 mV), as well as all directly synthesized Fe-based (oxy)hydroxides on NF and bare NF (Figure 2c). In fact, the attained activity was better than those of most recently reported binder-free TM-based catalysts supported by NF, which all reconstructed into real active TM-based (oxy)hydroxides during OER, as well as commercial Raney nickel catalyst (Table S2). Figure S17–S18 clearly ruled out the possible influence of Pt wire (counter electrode) and NF substrate for OER catalysis.^[32] Additionally, the OER kinetics were evaluated *via* Tafel slope measurements (Figure S19), where the value of post CA-CaFe₆Ge₆/NF was as low as 43.35 mV dec⁻¹, comparable to that of another reported active iron intermetallic OER catalyst obtained by the same steady-state method, implying its favorable kinetics process.^[28] This point was further affirmed *via* the electrochemical impedance spectroscopy (EIS) test for post CA-CaFe₆Ge₆/NF and various Fe-based (oxy)hydroxides on NF, from which post CA-CaFe₆Ge₆/NF shows the smallest charge-transfer resistance (R_{ct}) of around 2.18 Ω (Figure 2d and Table S3). Thus, the intermetallic CaFe₆Ge₆-derived Fe-based structure possessed a better ability of charge transfer. In addition, NF-supported post CA-CaFe₆Ge₆ presented the highest C_{dl} value compared with all the directly prepared Fe-based (oxy)hydroxides on NF, implying more exposed active sites on the surface were induced during the *in-situ* surface reconstruction (Figure S20). Inspired by the OER high activity, we conducted a stability test of post CA-CaFe₆Ge₆/NF at 1000 mA cm⁻² for 25 h that displayed a stable CA curve suggesting its practical importance (Figure S21). Moreover, the Faradaic efficiency (FE) of CaFe₆Ge₆ towards the OER process was determined as high as around 96% by comparing the experimentally measured amount of produced O₂ and the theoretically calculated one (Figure S22). Based on the above electrochemical evaluations, we conclude the intermetallic CaFe₆Ge₆-precatalyst is highly efficient for OER.

Ex-situ and in-situ post CA-characterizations

In order to confirm that the surface reconstruction of CaFe₆Ge₆ into the Ca–Fe–O heterostructure was induced by the anodic activation during the OER process, as well as to determine the specific composition of such *in-situ* transformed CaFeO_x, we carried out a series of characterizations employing both *in-situ* and *ex-situ* methods for CaFe₆Ge₆ after 24 h CA at 10 mA cm⁻² current density. In Figures S23–S24, the PXRD pattern and SEM images of post CA-CaFe₆Ge₆/NF illustrate that the CaFe₆Ge₆ phase was still preserved in its particle-like structure. In the SEM-associated EDX mapping, after the OER CA test, the co-

existence of Ca, Fe, and Ge on the surface of CaFe₆Ge₆ was dispersed inhomogeneously (Figure S25–S26), while the atomic ratio of these three elements determined by both ICP-AES and EDX (Table S4) revealed massive loss of Ge.^[27,29] The EDX analysis conducted after the CA sample further confirmed that surface Ge was dissolved into the electrolyte rather than redeposited on the counter (Pt) electrode (Figure S27). Conversely, most Ca remains in the system. To further determine the structural evolution of CaFe₆Ge₆ during OER, we conducted TEM measurements (HRTEM, SAED, and the associated EDX mapping) for the post CA-CaFe₆Ge₆. Figure 3a displayed the outer part of the post CA-CaFe₆Ge₆ particle turned out ultrathin and porous, which can be confirmed by its different amplified regions (Figure S28 and Figure 3b). This is in agreement with the above discussion where the bulk CaFe₆Ge₆ transformed into core (the remained CaFe₆Ge₆)-shell (reconstructed Ca–Fe–O) structure with high porosity through the leaching of Ge atoms.

To have a closer look at such a Ca–Fe–O shell that holds a sheet-like and porous features of OER transformed (oxy)hydroxides,^[6,33] the HRTEM was intentionally carried out for the identification of the lattice fringes. The (111) crystalline planes of α -Fe^{III}OOH with an interplanar spacing of 0.245 nm was determined (PDF #29-0713), while the lattice fringes of 0.213 nm can be assigned to the (008) plane of vaterite-phase CaCO₃ (PDF #33-0268) (Figure 3c). Besides, the interfaces between various facets of these two species were also apparent indicating their homogenous distribution (Figure S29). The composition of the Ca–Fe–O shell was further affirmed by the corresponding SAED pattern, in which the coupled facets of α -Fe^{III}OOH and vaterite can be well differentiated (Inset in Figure 3c). In order to reflect the distribution of different components in our system more intuitively, the high-angle annular dark-field scanning transmission electron microscopy (HAADF-STEM) and the relative EDX elemental mapping images are also shown in Figure 3d–g and Figure S30. On the one hand, in the bulk core region, the elements Ca, Fe, and Ge were still well-homogeneously distributed, manifesting the residual CaFe₆Ge₆ intermetallic core, which can facilitate the transport of charges. On the other hand, at the surface shell, only Fe, Ca, and O can be found but no Ge. The above results demonstrated the transformation of intermetallic precatalyst during OER into a porous Ca–Fe–O shell composed of α -Fe^{III}OOH and vaterite-phase CaCO₃ with the leaching of Ge, forming a core-shell structure with the remaining CaFe₆Ge₆ core.

To gain more insight into such surface structural reconstruction and the composition of Ca–Fe–O shell, XPS, *ex-situ* and *in-situ* Raman, as well as infrared (IR) spectroscopic characterizations were performed for the post CA-CaFe₆Ge₆ sample. As shown in Figure 4a, the high-resolution Ca 2p_{3/2} XPS spectrum for CaFe₆Ge₆/NF after OER CA can be deconvoluted into two peaks. Remarkably, the characteristic peak for metallic Ca (at around 345.6 eV) was considerably weak, while the prominent peak can be ascribed to the presence of calcium carbonate (at around 347.9 eV).^[34,35] The high-resolution XPS spectrum of Fe 2p_{3/2} can be fitted to residual metallic Fe and Fe^{II} peaks (at around 706.9 and 708.8 eV, respectively), while the majority of Fe 2p_{3/2} can be deconvoluted into the peak positioned at

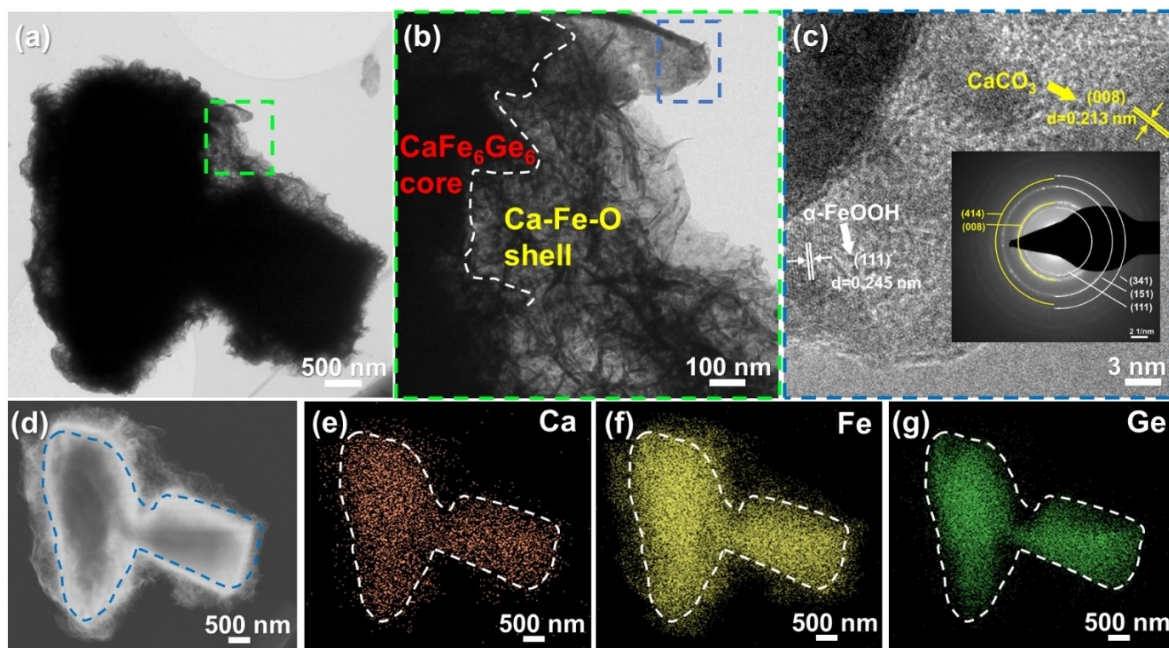


Figure 3. (a) The TEM images of post CA- CaFe_6Ge_6 particle and (b) its locally amplified area (the region marked with yellow frame in Figure 4a). (c) The HRTEM image focusing on the porous and thinner shell of the post CA-particle (the region marked with blue frame in Figure 4b) with an inset of the associated SAED pattern. (d) HAADF-STEM image of the post CA-particle, together with the relative EDX elemental mapping images for (e) Ca (orange), (f) Fe (yellow), and (g) Ge (green).

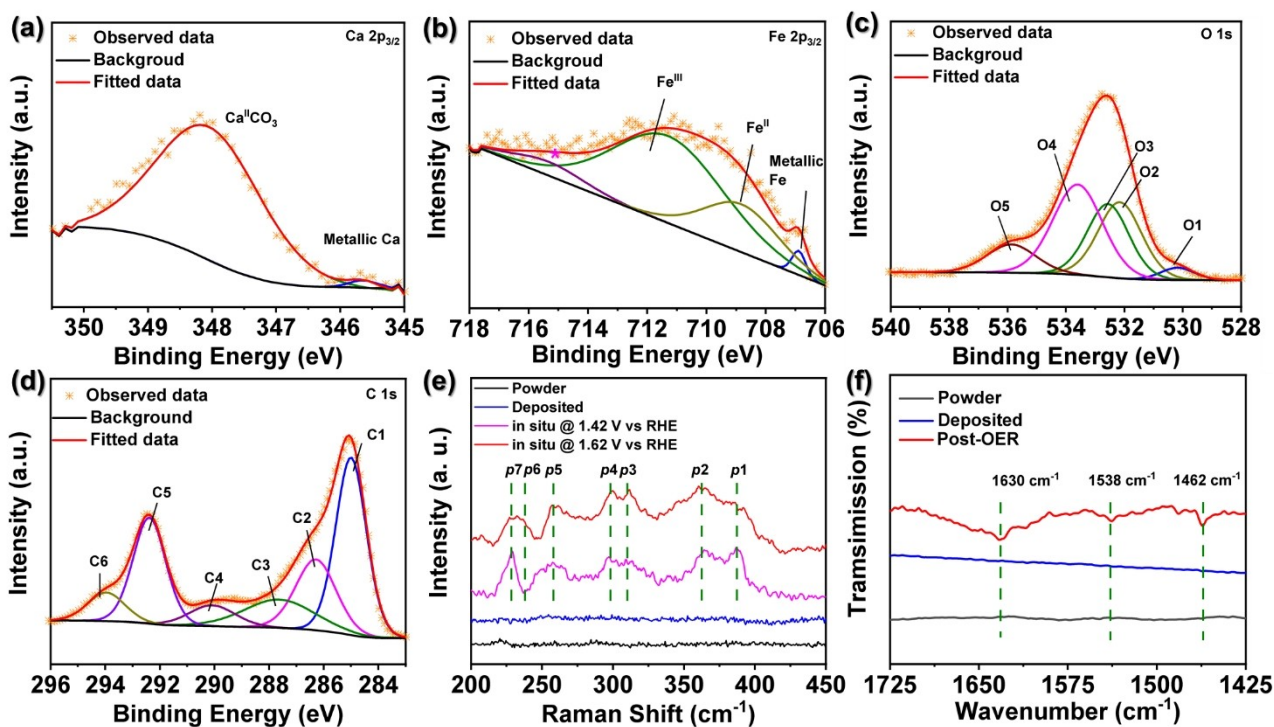


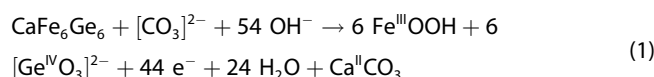
Figure 4. The deconvoluted high-resolution (a) $\text{Ca } 2p_{3/2}$, (b) $\text{Fe } 2p_{3/2}$, (c) $\text{O } 1s$, and (d) $\text{C } 1s$ XPS spectra of the post CA- $\text{CaFe}_6\text{Ge}_6/\text{NF}$. (e) Quasi *in-situ* Raman spectra of post CA- CaFe_6Ge_6 samples collected at 1.42 and 1.62 V (vs RHE) in 1 M KOH media. For comparison, the *ex-situ* Raman spectra of powder and deposited CaFe_6Ge_6 were also investigated. (f) Corresponding IR spectra of powder, deposited, and post OER- CaFe_6Ge_6 .

711.3 eV, which can be assigned to the presence of Fe^{III} oxyhydroxides (Figure 4b).^[25,36] Meanwhile, the Ge XPS spectrum in Figure S31 unveiled that the remained Ge mainly existed in the oxidized state (Ge^{IV} in GeO₃²⁻).^[27,29] The formation of calcium carbonate and Fe^{III} oxyhydroxides on the surface of CaFe₆Ge₆ can be further evidenced by O 1s XPS. As depicted in Figure 4c, five sub-peaks O1, O2, O3, O4, and O5 can be well-fitted at 530.1, 532.1, 532.5, 533.6, and 535.8 eV, respectively. Both O1 and O2 peaks correspond to the existence of lattice oxygen in α-Fe^{III}OOH,^[37] while O3 and O4 are related to the C=O and C–O in CaCO₃, respectively.^[38,39] Moreover, the additional apparent O5 peak arises from the Nafion binder.^[40] We further analyzed the C 1s XPS peak to confirm and obtain more information on the *in-situ* formed CaCO₃. Figure 4d showed that the C 1s XPS spectrum can be fitted to six sub-peaks (C1–C6), among which C2 (at around 286.3 eV) and C3 (at around 287.6 eV) can be indexed to the C–O in calcium carbonate.^[41,42] In particular, the peaks of C1 (285 eV) and C4 (290.1 eV) were reported in the case of vaterite-phase CaCO₃, corresponding to the C–C bond, as well as CO₃²⁻, respectively.^[41,43] Note another two C1s peaks (C5 and C6) were non-negligible, which both resulted from the utilization of the Nafion binder.^[44]

Furthermore, deeper investigation into the *in-situ* reconstructed porous Ca–Fe–O (vaterite-phase CaCO₃ coupled with α-Fe^{III}OOH) heteroshell could also be achieved using a combination of *ex-situ* and *in-situ* Raman spectroscopy, supplemented by IR measurements. During the OER CA process, the NF substrate might also participate in the reaction through oxidation into the Fe-doped Ni-based (oxy)hydroxides,^[28,45] which can interfere with the analysis of the Raman and IR spectroscopic data while monitoring the structural reconstruction of CaFe₆Ge₆ during water oxidation. Thus, we deposited the CaFe₆Ge₆ precatalyst on electrochemically inert carbon paper (CC). More importantly, we freeze quenched (–196 °C) the post CA (at an applied potential of 10 mA cm⁻² for 24 h) CaFe₆Ge₆/CC during the CV (Figure S32) at a potential located in the redox peak onset (1.42 V vs RHE) and one during substantial OER (1.62 V vs RHE). In Figure 4e, between 200 and 400 cm⁻¹, both powder and deposited CaFe₆Ge₆ samples did not exhibit any Raman band, while several distinct peaks can be observed for both *in-situ* measured samples (denoted as *p1–p7*). In particular, when the applied potential was increased into the absolute OER region (1.62 V vs RHE), these characteristic bands were more pronounced. Specifically, Raman detectable vibrations *p6*, *p3*, and *p1* were located at around 238 (*w*), 309 (*s*), and 388 (*s*) cm⁻¹, respectively, which originated from the pure α-Fe^{III}OOH.^[25,46, 47] Further, the corresponding *p5* and *p2* peaks found at 257 and 362 cm⁻¹ were assigned to the various vibrational modes of FeO₆ octahedra.^[48,49] Contrarily, the *p4* (299 cm⁻¹) band can be attributed to a lattice vibration of CaCO₃ in the vaterite phase.^[50] Note that the band *p7* at around 228 cm⁻¹ in both *in-situ* samples derives from ice,^[51] which remained on the sample surface during freeze quenching at cryogenic temperatures.

Moreover, the IR spectroscopy was used to shed more light on the composition details of the reconstructed Ca species in the post CA-sample. Figure 4f illustrates that for the powder

and deposited CaFe₆Ge₆, no band can be found, while the sample after 24 h OER CA presented two distinct vibration bands centered at 1462 and 1538 cm⁻¹, as well as a broader absorption around 1630 cm⁻¹, which were characteristic for the anti-symmetric stretching of the vaterite-phase CaCO₃, in-plane bending vibration of the CO₃²⁻ ion, and deformation vibration of H₂O, respectively.^[43,52–54] Complementary, the IR results further revealed that such post OER remaining Ca species were calcium carbonates in the vaterite phase.^[52] Under ambient air, considerable dissolved carbonate ions were present in the alkaline electrolytes,^[29,55] which reacted with the exposed Ca atoms during the anodic activation, finally promoting the formation of vaterite CaCO₃. Thus, with the support of the Pourbaix diagram, we anticipate that the structural conversion proceeds through Equation (1) [Eq. (1)].^[29,56]

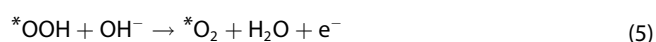


Insight into the effect of Ca and the possible reaction mechanism

So far, we have elaborated the first three research questions (i)–(iii) of the introduction in detail. Now, in order to investigate question (iv), we deliberately compared the OER activity of our CaFe₆Ge₆ with the previously reported Ca-free binary intermetallic Fe₆Ge₅ (Figure S33),^[27] as well as the same CaFe₆Ge₆ sample under a CO₂-free environment. First, the CaFe₆Ge₆ and Fe₆Ge₅ were deposited on glassy carbon electrodes (CaFe₆Ge₆/GCE and Fe₆Ge₅/GCE) and NF (CaFe₆Ge₆/NF and Fe₆Ge₅/NF) using Nafion binder (Figure S34–S37). The GCE was selected here because it is absolutely electrochemically inert, which can more intrinsically reflect the role of calcium species if present in water oxidation. As expected, for both GCE and NF-supported samples, their LSV, EIS, and C_{dl} results before CA activation (Figure S38–S43 and Table S5–S6) have comprehensively and clearly elaborated that the Ca-containing iron germanide showed distinctly diminished reaction overpotential and accelerated reaction kinetics. This is because a higher number of activated Fe atoms induced by the introduction of Ca participated in the OER process, which can be well-demonstrated by integrating the reduction peaks emerging in CV cycles of CaFe₆Ge₆/GCE and Fe₆Ge₅/GCE. Figure S44 presents that the number of redox-active Fe atoms potentially involved in the reaction for CaFe₆Ge₆ was nearly 4 times greater than for Fe₆Ge₅.^[6,11] Note that incorporation of Ca^{II} as Lewis acidic sites can facilitate the adsorption and activation of hydroxyl species in alkaline OER.^[21] On the other hand, Ca^{II} is redox-inactive and can assist the present redox-active TM (Fe) in the same system to provide more efficient catalytic sites rather than directly taking part in the catalytic process.^[57,58] Therefore, in the present case, the presence of Ca^{II} most likely allowed to adsorb more hydroxyls and then transferred them towards the nearby Fe sites for the subsequent OER steps. Accordingly, more Fe sites were involved as active sites with higher efficiency, which can

be further manifested by excellent turnover frequency (TOF), as well as the ECSA (C_{dl})-normalized and mass-normalized activity for $\text{CaFe}_6\text{Ge}_6/\text{GCE}$ (Table S7 and Figure S45).^[6,11,59] This explains why the Ca-containing iron germanide can transform into iron (oxy)hydroxides with a larger active surface area and enhanced catalytic activity than that of bimetallic iron germanide. Moreover, we further compared the OER activity of $\text{CaFe}_6\text{Ge}_6/\text{NF}$ in a CO_2 -free environment with that in normal ambient air. It turned out that both pre- and post-CA (at 10 mAcm^{-2} for 24 h) of $\text{CaFe}_6\text{Ge}_6/\text{NF}$ in a CO_2 -free environment exhibited inferior OER activity than those in ambient air (Figure S46). Furthermore, in a CO_2 -free 1 M KOH media, both EDX results, as well as the ICP-AES measurement unveiled that significantly more Ca leached out from the post CA- CaFe_6Ge_6 compared with the same sample working under ambient air (Figure S47–S48 and Table S8). This implied that, in a CO_2 -free environment, CaCO_3 was absent, thereby the needed functional Ca–Fe–O shell can hardly be constructed during the OER, leading to a drastic loss of OER activity. The absence of CaCO_3 in such post-OER CaFe_6Ge_6 sample was further verified by the IR characterization (Figure S49). Accordingly, this proves the important role of CaCO_3 in the OER activity enhancement.

To answer the last research question (v), one needs to look into the recent discovery that carbonates can promote the deprotonation of the reaction intermediates and the formation of O–O bonds.^[30,31] The existence of Lewis acid species (here Ca^{II}) can effectively adsorb and transport hydroxyls under alkaline OER process conditions,^[21] which then can accelerate and facilitate the alkaline OER efficiency.^[21,60, 61] Alternatively, the involved alkaline OER reaction steps are summarized in Equations (2–6) [Eq. (2–6)].^[32]



With this background, the following OER mechanism with the unprecedented Ca–Fe–O system can be rationally proposed: (i) apart from those hydroxyls directly adsorbed by Fe sites, more hydroxyls in the electrolyte were probably bound by the Ca^{II} ions; (ii) as Ca^{II} is redox-inactive and cannot directly participate in the catalysis,^[57,58] it tends to transfer the adsorbed hydroxyls towards the nearby redox-active Fe atoms, promoting their activity. Meanwhile, the carbonates substantially contributed to the deprotonation process, promoting the formation of intermediate $* \text{O}$ adsorbed on active Fe sites;^[30,31] (iii) The $* \text{O}$ intermediates further reacted with the additional hydroxyls, turning into the intermediate $* \text{OOH}$, and then (iv) CaCO_3 containing carbonates further dissociated the protons from the $* \text{OOH}$, finally facilitating the formation of desired O_2 molecules.

So far, we clarified the role of each component in our catalyst system. At the outermost region of precatalyst CaFe_6Ge_6 , Ge was leached out with the OER-induced surficial reconstruction, leaving a porous Ca–Fe–O layer, thus exposing more active sites and increasing high specific surface area. The Ca atoms elevated the mass transport and activated more Fe involved in the oxygen evolution, while carbonates sustainably deprotonated the intermediates, synergically promoting the formation of final O_2 . In the whole process, the redox-active Fe atoms acted as the catalytic sites. On the other hand, the residual intermetallic core can facilitate the electron transfer efficiency, compensating for the poor intrinsic electric conductivity of pure iron (oxy)hydroxides. Consequently, the cooperation of these components ensured the resulting high OER capability.

Conclusion

In conclusion, we have successfully addressed the research questions (i–v). To answer question (i), we synthesized and used the ternary intermetallic CaFe_6Ge_6 as a precatalyst for alkaline OER that transformed into a core (conductive CaFe_6Ge_6)-shell (Ca–Fe–O) heterostructure induced by anodic surface corrosion during the OER process. To determine the composition of such porous shell (answers to the question (ii) and (iii)), we utilized *in-situ* Raman spectroscopy, as well as comprehensive *ex-situ* characterization methods. The active structure for OER consisted of crystalline $\alpha\text{-Fe}^{III}\text{OOH}$ and vaterite-phase CaCO_3 . With regard to questions (iv) and (v), the important role of Ca^{II} on the improvement of the alkaline OER activity was confirmed by comparison of iron germanide with (ternary phase) and without Ca (binary phase) as precatalysts, as well as CaFe_6Ge_6 working in ambient air vs. CO_2 -free environment. Notably, the presence of CaCO_3 can promote the adsorption and transport of hydroxyl species, deprotonation of the OER reaction intermediates, as well as the eventual formation of O_2 . Meanwhile, benefiting from the remaining highly conducting intermetallic core, and the porous surface of the active catalyst with higher specific surface area and more exposed active sites caused by loss of Ge as GeO_3^{2-} , the *in-situ* transformed $\text{CaFe}_6\text{Ge}_6@ \text{Ca-Fe-O}$ on NF can drive 100 mAcm^{-2} at only 322 mV overpotential in 1 M KOH, surpassing the NF-supported noble metal-based catalyst, and all the directly prepared Fe-based (oxy)hydroxides. The presented detailed assessment and synergistic role of Ca towards the active Fe sites underlined the function and importance of redox inert metals (alkali and alkaline earth metals) in electrocatalytic systems that have often been neglected in the promotion of OER, especially from the perspective of structural reconstruction with flexible and varied components.

Experimental Section

Synthesis of CaFe_6Ge_6

For the synthesis of CaFe_6Ge_6 , arc melting has been performed using a modified Mini Arc Melting system (MAM-1, Johanna Otto GmbH) with a water-cooled copper-hearth in an argon-filled Glovebox (MBraun 20G, argon purity 99.996%). First, the iron and germanium pieces were pre-melted in a stoichiometric ratio of 1:1. Then 1.02 eq. of calcium was added. To avoid excessive evaporation of alkaline earth metal, melting was performed carefully and the sample turned several times. In the next step, the sample was sealed under vacuum in graphitized silica tubes and annealed at 1073 K in a muffle furnace (Nabertherm GmbH, Controller P330).

Synthesis of Fe_6Ge_5

Fe_6Ge_5 was synthesized using the same method as our previous report.^[27,62] Fe powder and Ge chips a ratio of 6:5 ratio were sealed into an evacuated quartz ampoule to be annealed at 1273 K for 2 days. And then, after grinding the as-obtained sample in an agate mortar, and pressing it into a pellet 8 mm in diameter, the sample was annealed again in a sealed and evacuated quartz ampoule at 923 K for 7 days.

Characterization

Various characterization methods, including PXRD, ICP-AES, SEM and TEM (coupled with EDX measurements), FT-IR, XPS, and *ex/in situ* Raman were employed, and details about these techniques can be found in the Supporting Information.

Electrochemical measurements

Electrochemical measurements were carried out in a standard three-electrode system in 1 M KOH controlled by a potentiostat (SP-200, BioLogic Science Instruments) controlled by the EC-Lab v10.20 software package. The catalysts deposited on different substrates were utilized as the working electrodes, and Pt wire (0.5 mm diameter \times 230 mm length; A-002234, BioLogic) and graphite carbon rod served as a counter electrode, and Hg/HgO worked as the reference electrode (CH Instruments, Inc.). To obtain the working electrodes, we firstly mixed 5 mg sample powder with 0.646 mL deionized water, 0.323 mL ethanol, and 0.03 mL Nafion, followed by ultrasonication of the mixture for 1 h. Afterward, the as-prepared homogeneous suspension was dipped on the well-polished glassy carbon electrode (GCE) with a diameter of 3 mm. The loading mass is around 1.429 mg cm^{-2} . Additionally, to deposit the catalyst powder on nickel foam (NF), Cu foam, and carbon paper, we immersed the bare metal foams and carbon paper into the as-prepared homogeneous suspension and dried it in the oven at 50 °C overnight. The resulting loading amount was around 3.5 mg cm^{-2} . Noble metal IrO_2 catalyst was deposited on NF as a reference using the same method. CV, LSV, CA experiments were carried out with an applied *iR* compensation of 85%. The uncompensated resistance (*R*_u) was obtained by an electrochemical impedance measurement at 100 MHz and potential of 1.175 V vs. RHE prior to each experiment. And 85% of *R*_u was used for the *iR* compensation, which was conducted by the software of the electrochemical workstation. The CV and LSV test for OER was performed at a scan rate of 5 mV s^{-1} . All measured potentials were calibrated with respect to RHE based on the following equation: $E(\text{RHE}) = E(\text{Hg}/\text{HgO}) + 0.098 \text{ V} + (0.059 \times \text{pH}) \text{ V}$, where the pH value of 1 M KOH was utilized from our previous report.^[63] Tafel slopes were determined by steady-state measurements through CA with a

stable potential for 5 min from with an interval of 15 mV. The average current values obtained at each potential were used for the calculation of Tafel plots.^[64] The Tafel slope was determined according to the Tafel equation: $\eta = b \log j + a$, in which η , b , and j represent overpotential (V), Tafel slope (mV dec^{-1}), and current density (mA cm^{-2}), respectively. To assess the electrochemical double-layer capacitance (C_{dl}), CV was performed at a non-Faradaic voltage region. The half of the difference of current density at the middle point of the CV cycle potential region was plotted as a function of the scan rate, producing the corresponding slope, which is the specific value of C_{dl} . The electrochemically active surface area (ECSA) can be then attained using the equation: $\text{ECSA} = C_{\text{dl}}/C_s$, in which C_s refers to the specific capacitance of the material per unit area under identical electrolyte conditions. Given that C_{dl} is linearly proportional to ECSA, we have normalized the current values to their C_{dl} .^[11] The electrochemical impedance spectroscopy (EIS) was recorded at 1.67 V (vs RHE) for GCE, as well as 1.515 and 1.53 V (vs RHE) for NF to attain the Nyquist plots. The amplitude of the sinusoidal wave was determined in a frequency range of 100 kHz to 1 mHz. The charge transfer resistance (R_{ct}) was reflected by the diameter of the semicircle in the Nyquist plots.^[28]

The Faradic efficiency (FE) was calculated by comparing the amount of experimentally produced H_2 and that of theoretically calculated gas according to the Faradic equation: $\text{FE} = (4 * V * F) / (V_m * Q)$. V represents the volume of experimentally evolved O_2 (mL), F represents the Faraday constant (96485 C mol^{-1}), V_m represents the molar volume (24.5 L mol^{-1} , RT), and Q represents the total amount of electrical charge (C). The amount of evolved gas was measured by the drainage method at a constant current of 50 mA for 3600 s.^[27] The TOF means the moles of O_2 per moles of total metal content (Fe in our case) evolved per second (s^{-1}). The TOF of electrocatalysts were calculated from the equation $\text{TOF} (\text{s}^{-1}) = (j \times N_A) / (z \times F \times n)$, where j represents the OER current density (A cm^{-2}), N_A represents the Avogadro number (6.02×10^{23}), F represents the Faraday constant (96485 C mol^{-1}), $z = 4$ for OER, n is the number of electrochemically active Fe which participated the water oxidation reaction.^[11,65]

Acknowledgements

Funded by the Deutsche Forschungsgemeinschaft (DFG, German Research Foundation) under Germany's Excellence Strategy – EXC 2008/1 – 390540038 – UniSysCat and the German Federal Ministry of Education and Research (BMBF project “Prometh2eus”, 03HY105C). P. W. M. greatly acknowledges support from the German Federal Ministry of Education and Research in the framework of the project Catlab (03EW0015A/B). The authors are indebted to Dr. Indranil Mondal for SEM, the group of Prof. Dr. Martin Lerch for XRD, Dr. Vitaly Gutkin for XPS analysis, as well as Prof. Dr. Andrei V. Shevelkov for providing the reference Fe_6Ge_5 . H. Y. thanks China Scholarship Council (CSC) for the Ph.D. fellowship. J. N. H. and K. L. are indebted to the Einstein Foundation Berlin/EC2/BIG-NSE for Ph.D. fellowships. Open Access funding enabled and organized by Projekt DEAL.

Conflict of Interest

The authors declare no conflict of interest.

Data Availability Statement

The data that support the findings of this study are available from the corresponding author upon reasonable request.

Keywords: calcium carbonate · electrocatalytic water oxidation · heterostructure · intermetallic germanides · structural reconstruction

- [1] C. Panda, P. W. Menezes, S. Yao, J. Schmidt, C. Walter, J. N. Hausmann, M. Driess, *J. Am. Chem. Soc.* **2019**, *141*, 13306–13310.
- [2] P. W. Menezes, C. Panda, C. Walter, M. Schwarze, M. Driess, *Adv. Funct. Mater.* **2019**, *29*, 1808632.
- [3] H. Yang, Z. Chen, P. Guo, B. Fei, R. Wu, *Appl. Catal. B* **2020**, *261*, 118240.
- [4] Z. Chen, H. Qing, R. Wang, R. Wu, *Energy Environ. Sci.* **2021**, *14*, 3160–3173.
- [5] H. Yang, J. Liu, Z. Chen, R. Wang, B. Fei, H. Liu, Y. Guo, R. Wu, *Chem. Eng. J.* **2021**, *420*, 127671.
- [6] H. Yang, G. Dai, Z. Chen, J. Wu, H. Huang, Y. Liu, M. Shao, Z. Kang, *Small* **2021**, *17*, 2101727.
- [7] C. Walter, P. W. Menezes, M. Driess, *Chem. Sci.* **2021**, *12*, 8603–8631.
- [8] W. Hao, D. Yao, Q. Xu, R. Wang, C. Zhang, Y. Guo, R. Sun, M. Huang, Z. Chen, *Appl. Catal. B* **2021**, *292*, 120188.
- [9] P. W. Menezes, C. Walter, J. N. Hausmann, R. Beltrán-Suito, C. Schlesiger, S. Praetz, V. Y. Verchenko, A. V. Shevelkov, M. Driess, *Angew. Chem. Int. Ed.* **2019**, *58*, 16569–16574; *Angew. Chem.* **2019**, *131*, 16722–16727.
- [10] H. Chiu, W. Huang, L. Hsu, Y. Lin, Y. Lai, C. Lin, *Sustain. Energy Fuels* **2018**, *2*, 271–279.
- [11] P. W. Menezes, C. Walter, B. Chakraborty, J. N. Hausmann, I. Zaharieva, A. Frick, E. v. Hauff, H. Dau, M. Driess, *Adv. Mater.* **2021**, *33*, 2004098.
- [12] Z. Jin, A. J. Bard, *Angew. Chem. Int. Ed.* **2021**, *60*, 794–799; *Angew. Chem.* **2021**, *133*, 807–812.
- [13] M. Wiechen, I. Zaharieva, H. Dau, P. Kurz, *Chem. Sci.* **2012**, *3*, 2330–2339.
- [14] M. M. Najafpour, T. Ehrenberg, M. Wiechen, P. Kurz, *Angew. Chem. Int. Ed.* **2010**, *49*, 2233–2237; *Angew. Chem.* **2010**, *122*, 2281–2285.
- [15] Yamada, M. Kinoshita, S. Oda, H. Tsukasaki, S. Kawaguchi, K. Oka, S. Mori, H. Ikeno, S. Yagi, *Chem. Mater.* **2020**, *32*, 3893–3903.
- [16] Yamada, H. Fujii, A. Takamatsu, H. Ikeno, K. Wada, H. Tsukasaki, S. Kawaguchi, S. Mori, S. Yagi, *Adv. Mater.* **2017**, *29*, 1603004.
- [17] D. González-Flores, I. Zaharieva, J. Heidkamp, P. Chernev, E. Martínez-Moreno, C. Pasquini, M. R. Mohammadi, K. Klingan, U. Gernet, A. Fischer, H. Dau, *ChemSusChem* **2016**, *9*, 379.
- [18] S. Y. Lee, D. González-Flores, J. Ohms, T. Trost, H. Dau, I. Zaharieva, P. Kurz, *ChemSusChem* **2014**, *7*, 3442–3451.
- [19] Y. Mousazade, M. R. Mohammadi, R. Bagheri, R. Bikas, P. Chernev, Z. Song, T. Lis, M. Siczek, N. Noshiranzadeh, S. Mebs, H. Dau, I. Zaharieva, M. M. Najafpour, *Dalton Trans.* **2020**, *49*, 5597–5605.
- [20] Z. N. Zahran, E. A. Mohameda, Y. Naruta, *J. Mater. Chem. A* **2017**, *5*, 15167–15174.
- [21] Z. Sun, Y. Wang, L. Lin, M. Yuan, H. Jiang, R. Long, S. Ge, C. Nan, H. Li, G. Sun, X. Yang, *Chem. Commun.* **2019**, *55*, 1334–1337.
- [22] S. Yao, V. Forstner, P. W. Menezes, C. Panda, S. Mebs, E. M. Zolnhofer, M. E. Miehlich, T. Szilvasi, N. A. Kumar, M. Haumann, K. Meyer, H. Grützmacher, M. Driess, *Chem. Sci.* **2018**, *9*, 8590–8597.
- [23] C. Panda, P. W. Menezes, C. Walter, S. Yao, M. E. Miehlich, V. Gutkin, K. Meyer, M. Driess, *Angew. Chem. Int. Ed.* **2017**, *56*, 10506–10510; *Angew. Chem.* **2017**, *129*, 10642–10646.
- [24] R. Beltrán-Suito, V. Forstner, J. N. Hausmann, S. Mebs, J. Schmidt, I. Zaharieva, K. Laun, I. Zebger, H. Dau, P. W. Menezes, M. Driess, *Chem. Sci.* **2020**, *11*, 11834–11842.
- [25] B. Chakraborty, R. Beltrán-Suito, J. N. Hausmann, S. Garai, M. Driess, P. W. Menezes, *Adv. Energy Mater.* **2020**, *10*, 2001377.
- [26] M. W. Louie, A. T. Bell, *J. Am. Chem. Soc.* **2013**, *135*, 12329–12337.
- [27] J. N. Hausmann, R. A. Khalaniya, C. Das, I. Remy-Speckmann, S. Berendts, A. V. Shevelkov, M. Driess, P. W. Menezes, *Chem. Commun.* **2021**, *57*, 2184.
- [28] J. N. Hausmann, R. Beltrán-Suito, S. Mebs, V. Hlukhyy, T. F. Fässler, H. Dau, M. Driess, P. W. Menezes, *Adv. Mater.* **2021**, *33*, 2008823.
- [29] P. W. Menezes, S. Yao, R. Beltrán-Suito, J. N. Hausmann, P. V. Menezes, M. Driess, *Angew. Chem.* **2021**, *133*, 4690–4697; *Angew. Chem. Int. Ed.* **2021**, *60*, 4640–4647.
- [30] K. Aiso, R. Takeuchi, T. Masaki, D. Chandra, K. Saito, T. Yui, M. Yagi, *ChemSusChem* **2017**, *10*, 687–692.
- [31] Mizrahi, D. Meyerstein, *Adv. Inorg. Chem.* **2019**, *74*, 343–360.
- [32] H. Yang, M. Driess, P. W. Menezes, *Adv. Energy Mater.* **2021**, *11*, 2102074.
- [33] J. N. Hausmann, S. Mebs, K. Laun, I. Zebger, H. Dau, P. W. Menezes, M. Driess, *Energy Environ. Sci.* **2020**, *13*, 3607–3619.
- [34] P. Selvam, B. Viswanathan, V. Srinivasan, *J. Electroanal. Chem.* **1989**, *257*, 203–211.
- [35] H. Bala, Y. Zhang, H. Yang, C. Wang, M. Li, X. Lv, Z. Wang, *Colloids Surf. A: Physicochem. Eng. Asp.* **2007**, *294*, 8–13.
- [36] L. Wu, L. Yu, B. McElhenny, X. Xing, D. Luo, F. Zhang, J. Bao, S. Chen, Z. Ren, *Appl. Catal. B* **2021**, *294*, 120256.
- [37] B. Kim, J. Park, W. Choi, D. Han, J. Kim, H. Park, *Appl. Catal. B* **2021**, *283*, 119608.
- [38] S. Sabbarwal, A. K. Dubey, M. Pandey, M. Kumar, *J. Mater. Chem. B* **2020**, *8*, 5729–5744.
- [39] L. Liao, X. Cheng, Y. Ma, P. Zuo, W. Fang, G. Yin, Y. Gao, *Electrochim. Acta* **2013**, *87*, 466–472.
- [40] D. Ramdutt, C. Charles, J. Hudspeth, B. Ladewig, T. Gengenbach, R. Boswell, A. Dicks, P. Brault, *J. Power Sources* **2007**, *165*, 41–48.
- [41] H. Liu, X. Tian, M. Ouyang, X. Wang, D. Wu, X. Wang, *Renewable Energy* **2021**, *179*, 47–64.
- [42] S. Ren, B. Liu, G. Han, H. Zhao, Y. Zhang, *Nanoscale* **2021**, *13*, 12149–12156.
- [43] D. H. Chu, M. Vinoba, M. Bhagiyalakshmi II, H. Baek, S. C. Nam, Y. Yoon, S. H. Kim, S. K. Jeong, *RSC Adv.* **2013**, *3*, 21722.
- [44] J. L. Pineda-Delgado, C. Gutierrez, S. Rivas, N. Arjona, L. G. Arriaga, A. U. Chávez-Ramirez, *Nanotechnology* **2019**, *30*, 105707.
- [45] Y. J. Son, K. Kawashima, B. R. Wygant, C. H. Lam, J. N. Burrow, H. Celio, A. Dolocan, J. G. Ekerdt, C. B. Mullins, *ACS Nano* **2021**, *15*, 3468–3480.
- [46] D. L. A. de Faria, F. N. Lopes, *Vib. Spectrosc.* **2007**, *45*, 117–121.
- [47] C. Liang, P. Zou, A. Nairan, Y. Zhang, J. Liu, K. Liu, S. Hu, F. Kang, H. J. Fan, C. Yang, *Energy Environ. Sci.* **2020**, *13*, 86–95.
- [48] C. E. Camayo, S. Gaona, J. C. F. V. Raigoza, *J. Magn. Magn. Mater.* **2021**, *527*, 167733.
- [49] S. Singh, S. S. Menon, K. Gupta, R. Jayavel, *Mater. Lett.* **2014**, *131*, 332–335.
- [50] Y. Song, K. Yu, G. A. Ayoko, R. L. Frost, Q. Shi, Y. Feng, J. Zhao, *Spectrochim. Acta A Mol. Biomol. Spectrosc.* **2013**, *112*, 95–100.
- [51] V. Korepanov, C. Yu, H. Hamaguchi, *J. Raman Spectrosc.* **2018**, *49*, 1742–1746.
- [52] D. Gebauer, P. N. Gunawidjaja, J. Y. P. Ko, Z. Bacsik, B. Aziz, L. Liu, Y. Hu, L. Bergström, C. Tai, T. Sham, M. Edén, N. Hedin, *Angew. Chem. Int. Ed.* **2010**, *49*, 8889–8891; *Angew. Chem.* **2010**, *122*, 9073–9075.
- [53] Y. Suetsugu, I. Shimoya, J. Tanaka, *J. Am. Ceram. Soc.* **1998**, *81*, 746–748.
- [54] Z. Cheng, A. Yasukawa, K. Kandori, T. Ishikawa, *J. Chem. Soc. Faraday Trans.* **1998**, *94*, 1501–1505.
- [55] B. M. Hunter, W. Hieringer, J. R. Winkler, H. B. Gray, A. M. Müller, *Energy Environ. Sci.* **2016**, *9*, 1734–1743.
- [56] D. G. Brookins, *Eh-pH Diagrams for Geochemistry*, Springer, Berlin Heidelberg, **1988**.
- [57] J. S. Kanady, E. Y. Tsui, M. W. Day, T. Agapie, *Science* **2011**, *333*, 733–736.
- [58] E. Y. Tsui, T. Agapie, *Proc. Natl. Acad. Sci. USA* **2013**, *110*, 10084–10088.
- [59] J. Kibsgaard, I. Chorkendorf, *Nat. Energy* **2019**, *4*, 430–433.
- [60] P. Liu, B. Chen, C. Liang, W. Yao, Y. Cui, S. Hu, P. Zou, H. Zhang, H. J. Fan, C. Yang, *Adv. Mater.* **2021**, *33*, 2007377.
- [61] Y. Hong, K. M. Kim, J. H. Ryu, S. Mhin, J. Kim, G. Ali, K. Y. Chung, S. Kang, H. Han, *Adv. Funct. Mater.* **2020**, *30*, 2004330.
- [62] Z. Chen, H. Yang, Z. Kang, M. Driess, P. W. Menezes, *Adv. Mater.*, DOI: 10.1002/adma.202108432.
- [63] J. N. Hausmann, B. Traynor, R. J. Myers, M. Driess, P. W. Menezes, *ACS Energy Lett.* **2021**, *6*, 3567–3571.
- [64] S. Anantharaj, S. Noda, M. Driess, P. W. Menezes, *ACS Energy Lett.* **2021**, *6*, 1607–1611.
- [65] B. Chakraborty, R. Beltrán-Suito, V. Hlukhyy, J. Schmidt, P. W. Menezes, M. Driess, *ChemSusChem* **2020**, *13*, 3222–3229.

Manuscript received: February 28, 2022

Revised manuscript received: March 9, 2022

Accepted manuscript online: March 10, 2022

Version of record online: April 1, 2022